Kinetics-based design of a flow platform for highly reproducible on demand synthesis of gold nanoparticles with controlled size between 50-150 nm and their application in SERS and PIERS sensing

Luca Panariello[a], Ka Chuen To[b], Zhara Khan[b], Gaowei Wu[a], Georgios Gkogkos[a], Spyridon Damilos[a], Ivan P. Parkin[b], Asterios Gavriilidis[a].

a: Department of Chemical Engineering, University College London, Torrington Place, London WC1E 7JE, UK.

b: Department of Chemistry, University College London, 20 Gordon Street, London, WC1H 0AJ, UK

Abstract

Seeded-growth synthetic protocols enable precise control of particle size and shape, crucial for many sensing applications. However, scaling-up these syntheses in a reproducible way is challenging, as minimal variation in process parameters such as seed size, concentration or reaction temperature can significantly alter the final product. Flow reactors enable tight control in the process parameters and high reproducibility of the synthesis, representing a potential technology to perform seeded-growth synthesis in large scale. This work reports the design of a flow platform for the controlled synthesis of spherical gold nanoparticles with size up to $150\ \mathrm{nm}$ through a seeded-growth approach, and their use in Surface Enhanced Raman Scattering (SERS) and Photoinduced Enhanced Raman Spectroscopy (PIERS). The particle growth kinetics were studied via *in situ* time-resolved UV-Vis spectroscopy. The spectroscopic data were fitted with a kinetic model, which was subsequently used for the design of the reactor. The kinetics-based design approach enabled fast translation of the growth synthesis in flow, eventually allowing the on demand flow synthesis of particles with controllable size, ranging from 50 to $150\ \mathrm{nm}$, with high reproducibility and full precursor conversion. The particles were tested for SERS and PIERS for different substrates, including warfare agents and biomolecules, with enhancement factors between 10^3 and 10^8 depending on the analyte, demonstrating their potential for detection of various analytes.

Introduction

Gold nanoparticles (Au NPs) represent a topic of intense research in several areas, comprising optics [1], biomedicine [2,3] and catalysis [4,5]. Their applications are strongly size dependent, with protocols available in the literature enabling the synthesis of particles from the sub-nanometer scale [6] up to hundreds of nanometers [7]. The reproducible synthesis of spherical gold nanoparticles above $20\ \mathrm{nm}$ with narrow size distribution ($\sim 10\%$ relative standard deviation) still remains a challenging task, as most protocols available in the literature comprise seeded-growth syntheses [8–13], with potential multiple reactant injections, which are highly operator-dependent. Various sources of irreproducibility can compromise the synthesis, particularly regarding possible variation of initial seed size and seed number concentration, as well as timing in reactants injection. These problems are exacerbated when scaling up the production using conventional batch technologies, since issues linked to nonuniform mixing and inhomogeneous temperature profile significantly affect batch reactors as their scale increases. During recent years, flow reactors appeared as a viable technology for the synthesis and scale up of nanomaterials production [14–16]. Several groups employed these type of reactors for the synthesis of gold nanoparticles, via single step syntheses [17–21] or seeded-growth protocols [16,22,23]. Despite the advancement in the field of flow synthesis of nanomaterials, only few examples of nanoparticle size control over a broad range within the same flow platform exist. Deshpande and Kulkarni [24] reported the synthesis of silver nanoparticles in size range between 65 and $120\ \mathrm{nm}$ using a cascade of CSTRs, however producing particles with broad size distribution. More recently, Pinho and Torrente-Murciano [25] reported the synthesis of silver nanoparticles with average size between 5 and $80\ \mathrm{nm}$ in a millifluidic reactor. This system required up to 5 precursor injections in order to achieve the largest average size, with particle size distribution relative standard deviation in the order of $\sim 10 - 20\%$

Plasmonic gold nanoparticles, particularly with size above $20\ \mathrm{nm}$, find applications in several sensing technologies, including lateral flow immunoassays [26] and surface enhanced Raman spectroscopy

(SERS) [27]. SERS is a highly sensitive technique capable of single molecule detection [28], with minimal sample preparation. It is a non-destructive and very fast analysis, which has been successfully used in a range of applications including medical diagnostics, [29] environmental monitoring[30] and chemical threats detection [31,32]. The SERS effect arises when an analyte molecule adsorbs onto a rough plasmonic metallic surface, leading to enhancement of the analyte Raman signal. In practice, this is achieved using nanostructured surfaces or nanoparticles. Metals such as silver and gold have been extensively used as SERS substrates, due to their stability, biocompatibility [33] and control of the optical properties [34]. The two main contributions to the SERS enhancement are the electromagnetic (EM) and the chemical enhancement (CE) factors, with the greatest contribution attributed to the former [35–37]. The EM enhancement arises from the electromagnetic interaction of light with the nanoparticle, leading to collective oscillations of surface conduction electrons of the nanoparticle called localised surface plasmon resonance (LSPR) [38]. This phenomenon leads to an enhancement of the electric field near the metal nanoparticle surface, in turn leading to enhancements of both the incident and Raman-scattered fields. The CE factor involves specific interactions between the analyte and the surface of the nanoparticle. Different mechanisms have been proposed for the CE, the most accredited being the charge-transfer mechanism. This mechanism involves charge transfer processes between the substrate and analyte [28,39]. SERS substrates can be broadly divided in three categories [40]: (1) nanostructures made through lithographic techniques, where the metal is deposited on the substrate using top-down approaches; (2) nanoparticles assembled on surfaces through a bottom-up approach; (3) nanoparticles in suspension. The first category relates to SERS substrates with the most regular structures. However, their (lithographic) production is difficult to scale-up, making them more expensive. Substrates belonging to both categories (2) and (3) are cheaper and easier to produce, thus appear to be a better candidate for the in-field application of SERS, especially as an inexpensive point-of-care diagnostic tool. As these kinds of substrates rely on the use of colloidal plasmonic particles, a critical aspect for their development is the availability of highly reproducible methods generating monodisperse nanoparticles. Flow

technologies can address this challenge, as they lead to improved nanomaterials synthesis reproducibility [41]. A currently developing area in the field of SERS is the combination of metallic nanoparticles with photo-activated substrates. This new technique, named photo-induced enhanced Raman spectroscopy (PIERS), has also opened up the possibility of reusable and self-cleaning substrates [42,43], both desirable qualities for the progression of SERS towards in-field applications.

In this work, we exploit the advantages offered by flow reactors to reproducibly grow preformed gold seeds, leading to the controllable synthesis of monodisperse particles with size between 50 and $150\ \mathrm{nm}$ using a single growth step. The developed system allows on demand synthesis of multiple sizes of nanoparticles by simply tuning the seeds inlet concentration. Following our recent work on continuous synthesis of Au nanoparticles [41], we designed the flow reactor presented in this work starting from the synthesis kinetics, studied (in batch) via *in situ* time-resolved UV-Vis spectroscopy. The batch-derived kinetics were modelled using a first-order kinetic rate, which is then used to rapidly determine the operating conditions of the reactor. The system here reported enables tight control over the particle size, achieving extremely high reproducibility in the synthesis product ($\sim 1\%$ variation in the particle size between different reactor runs). Among the particles produced, the $50\ \mathrm{nm}$ ones were employed for SERS and PIERS detection of various analytes. The produced particles appeared as versatile substrates, allowing detection of a variety of different molecules including warfare agents and biomolecules. We report successful detection of the reference molecule mercaptobenzoic acid (MBA), as well as more challenging analytes including the biomolecules glutathione and glucose and military explosives (RDX, 2,4,6-Trinitrotoluene (TNT), 2,2-Bis[(nitrooxy)methyl]-1,3-propanediol Dinitrate (PETN) and tetryl).

Experimental

Materials

Gold (III) chloride trihydrate ($HAuCl_4 \cdot 3\ H_2O, \geq 99.9\%$), Tris base (Trizma® base, $\geq 99\%$), hydrogen peroxide (30 wt.% in H_2O, ACS reagent), citric acid monohydrate (ACS reagent grade $\geq 99.0\%$) heptane (anhydrous, 99%), methanol (HPLC grade, 99.8 %), 2-propanol (laboratory reagent grade), ethanol (HPLC grade), water (HPLC grade), tepol, acetone (HPLC grade, 99.7%), titanium (IV) ethoxide (reagent grade, 97%), toluene (HPLC, 99.8%), 4-mercaptobenzoic acid (MBA, 99%), glutathione ($\geq 98\%$) and glucose (anhydrous, 96%) were purchased from Sigma-Aldrich. Accustandard explosives reference solutions (RDX, 2,4,6-Trinitrotoluene (TNT), 2,2-Bis[(nitrooxy)methyl]-1,3-propanediol Dinitrate (PETN) and tetryl) were purchased from Kinesis. All the reagents were used as supplied.

Nanoparticles characterization

Transmission electron microscopy (TEM) images of the particles were taken on a JEOL 2100 EXii microscope with 120 kV acceleration voltage. UV-Vis spectra of the colloidal solutions were acquired using an Ocean Optics Spectrophotometer (USB 2000+UV-Vis). For *in situ* time-resolved measurements, the reactions were carried out in a quartz cuvette (10 mm optical path, Hellma Optics), using a cuvette holder equipped with a magnetic stirrer (qpod, Quantum Northwest, stirring speed 3000 rpm). The synthesis conversion was measured via microwave plasma atomic emission spectroscopy (MP-AES). A given volume of gold nanoparticles colloid was mixed with an equal volume of a solution of NaCl (0.9 M) and HCl at pH 1 to cause particle flocculation. Then, part of the solution was filtered through a 0.2 µm syringe filter. The original solution and the filtered solution were digested in aqua regia (HNO_3: HCl $1:3$ v: v), and then analyzed using an Agilent 4210 MP-AES optical emission spectrometer, respectively providing the Au(III) concentration at the reactor inlet, $C_{\mathrm{Au(III)},0}$, and the Au(III) concentration at the reactor outlet, $C_{\mathrm{Au(III)},\tau}$. The conversion was calculated as $X = (C_{\mathrm{Au(III)},0} - C_{\mathrm{Au(III)},\tau})/C_{\mathrm{Au(III)},0}$.

Flow synthesis of 11 nm Au seeds

11 nm gold seeds were prepared using a segmented flow reactor according to previously published work [41]. In brief, $1\ \mathrm{mL}$ stock solution of $8\ \mathrm{mM\ Au(III)}$ precursor was prepared by diluting $320\ \mu\mathrm{L}$ of $25\ \mathrm{mM\ HAuCl_4}$ in $572\ \mu\mathrm{L}$ of deionised (DI) water ($15\ \mathrm{M\Omega\ cm}$). Then, $108\ \mu\mathrm{L}$ of $2\ \mathrm{M\ NaOH}$ were added, and the solution was kept in the fridge ($\sim 4\ ^\circ\mathrm{C}$) overnight. This stock was then diluted to $0.4\ \mathrm{mM\ Au(III)}$ with DI water. Two $25\ \mathrm{mL}$ glass syringes (Scientific Glass Engineering) were filled with the $0.4\ \mathrm{mM\ Au(III)}$ solution and a $4.8\ \mathrm{mM}$ solution of citric acid, and then placed in a syringe pump (KD Scientific Legato® 200). These two solutions were mixed in a first T-junction ($0.5\ \mathrm{mm}$ internal diameter (I.D.), Upchurch), then segmented with heptane in a second T-junction ($0.5\ \mathrm{mm}$ I.D., Upchurch) and entered a $6\ \mathrm{mL}$ polytetrafluoroethylene (PTFE) coil ($1\ \mathrm{mm}$ I.D., $10\ \mathrm{cm}$ radius of curvature, Thames Restek) at a temperature of $90\ ^\circ\mathrm{C}$. The flow rates were adjusted for the reactants to spend an average residence time of $7\ \mathrm{min}$ in the coil. This synthesis led to $11\ \mathrm{nm}$ seeds with narrow particle size distribution (relative standard deviation of the distribution of 10% based on TEM), as shown in Fig. S1. The particles were then collected and stored at $4\ ^\circ\mathrm{C}$ for further use.

In situ time-resolved UV-vis spectroscopy of growth experiments

The synthesis protocol was adapted from Li *et al.* [7] with minor changes. The produced $11\ \mathrm{nm}$ seeds were diluted to different concentrations with DI water to a total volume of $1.3945\ \mathrm{mL}$. This solution was pipetted to a stirred quartz cuvette with UV-Vis monitoring. Then, $0.0375\ \mathrm{mL}$ of a $100\ \mathrm{mM}$ stock of Tris base was added, followed by the addition of $0.0375\ \mathrm{mL}$ of $25\ \mathrm{mM}$ a stock solution of $\mathrm{HAuCl_4}$. After 1 min, $0.0305\ \mathrm{mL}$ of $\mathrm{H_2O_2}$ stock ($30\ \%_{wt}$) was added. The concentration of $\mathrm{Au(0)}$ atoms in the seeds after all the reactants were added in the three experiments performed was 0.007, 0.0008 and $0.00025\ \mathrm{mM}$ respectively. The spectra evolution was recorded with an acquisition time of $1\ \mathrm{s}$.

Flow growth of Au seeds

The growth process was translated in flow using the kinetics acquired in the UV-Vis spectroscopy experiments. The experimental set-up employed for the flow growth of the seeds comprised:

- a polyether ether ketone (PEEK) T-junction (0.5 mm I.D., Upchurch), where a solution of Au seeds (11 nm, concentration of $\mathrm{Au}(0)$ varying between 0.021 - 0.00075 mM depending on the desired size) and Tris base (7.5 mM) was mixed with a solution of $\mathrm{Au(III)}$ precursor (1.875 mM);
- a second PEEK cross junction (0.5 mm I.D., Upchurch), where the outlet of the PEEK T-junction was mixed with a water solution of $\mathrm{H_2O_2}$ (1.845 $\%_{wt}$), and segmented with heptane;
- a 10 mL polytetrafluoroethylene (PTFE) coil (2.4 mm I.D., 10 cm radius of curvature, Thames Restek) providing the residence time required for growth completion.

The solutions containing seeds and Au precursor were pumped with the aid of a syringe pump (KD Scientific Legato® 200), using disposable plastic syringes. The aqueous solution of $\mathrm{H_2O_2}$ and heptane were pumped using piston pumps (Milligat, Global FIA). The $\mathrm{H_2O_2}$ reservoir was kept in an ice bath to limit its degradation. A schematic of the set-up is provided in Fig. 1. The flow rates of $\mathrm{Au(III)}$, Au seeds and Tris base and $\mathrm{H_2O_2}$ were equal (0.055 mL/min). The heptane flow rate was set equal to the sum of the three aqueous flow rates (0.165 mL/min). The outlet of the reactor was connected to a three-way valve that directed the flow either to a waste vial or a collection vial. During reactor start-up, the flow was directed to the waste vial. Once steady state was reached (after an operating time equal to three times the nominal residence time of the reactor), the flow exiting the reactor was directed to the collection vial.

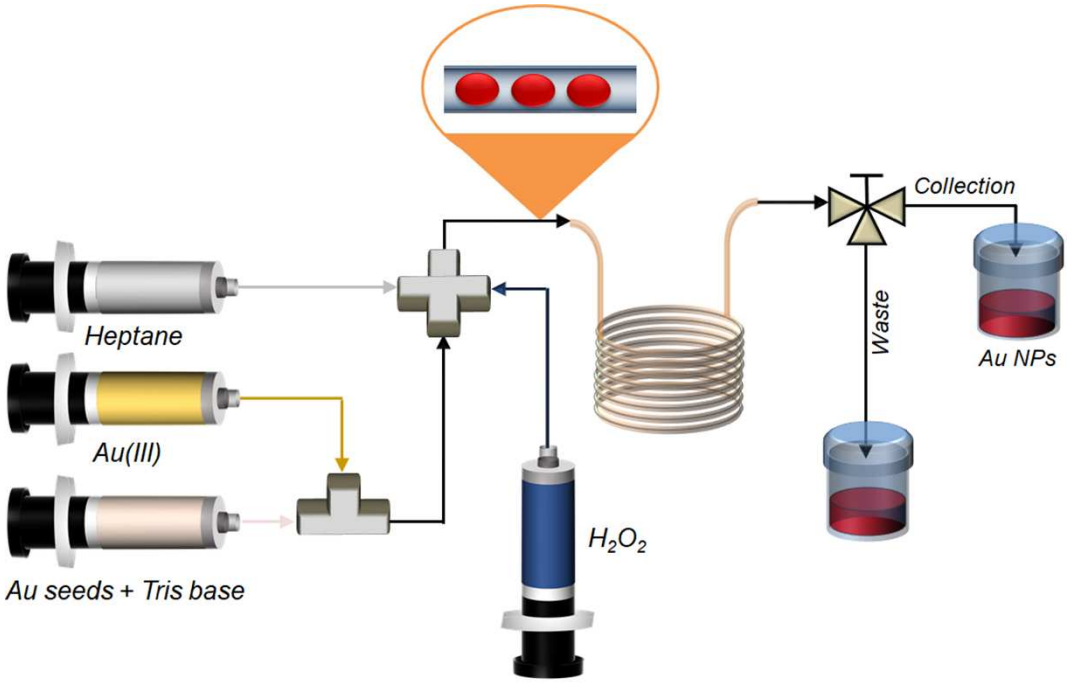

Figure 1. Schematic of the experimental set-up employed in the continuous growth synthesis of Au nanoparticles

SERS and PIERS measurements

A 100 mM stock solution of MBA was prepared in methanol. The stock solution was serially diluted using methanol to produce subsequent solutions with concentrations of 10 µM, 1 µM and 100 nM. Solutions of explosives were diluted as required with the same solvents as received. SERS and PIERS measurements were carried out on a Renishaw Raman inVia microscope with a 633 nm He-Ne excitation laser (1.9 mW when operated at 25% power, spot size approx. 4.4 µm^2). A minimum of 3 points were measured for each sample to ensure consistency between locations. For SERS measurements Au NPs and analyte solutions were vortexed in a 1:1 volumetric ratio, and 20 µL of this solution was deposited onto a glass microscope slide and allowed to dry before analysis. The Raman analysis was performed on the solid sample obtained after the solution dried. For PIERS, 20 µL of Au NPs/analyte mixture was deposited onto a TiO_2 thin film prepared using aerosol-assisted chemical vapour deposition (AACVD) and irradiated under UV-C light (254 nm, UVITec LI-215 G) for a

minimum of 2 h. The experimental protocols followed for both SERS and PIERS measurement are illustrated in Fig. 2.

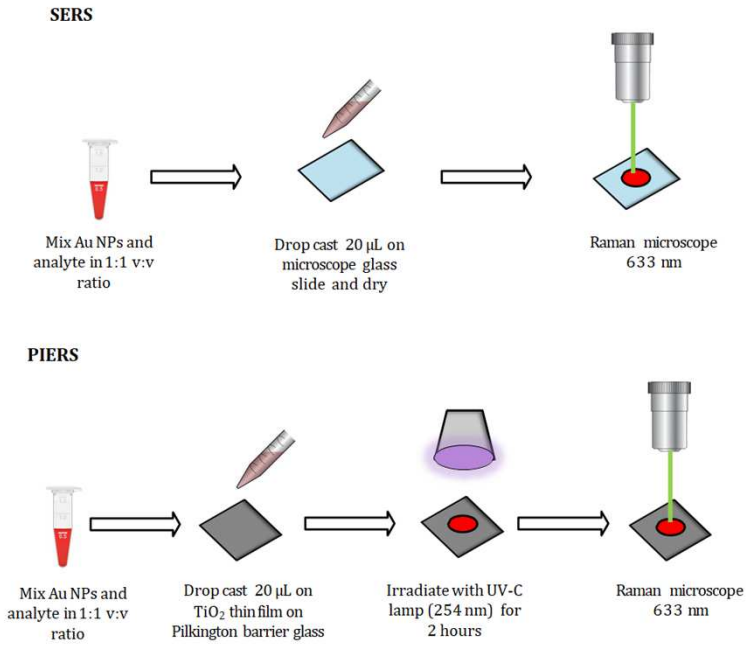

Figure 2. Experimental protocols followed for SERS (top) and PIERS (bottom) measurements.

The film used for PIERS measurements was prepared as follows: Pilkington barrier glass was used as the substrate material and deposition was carried on the atmospheric side of the glass to prevent leaching of ionic impurities from the glass. The glass slides were cleaned using tepol, isopropyl alcohol (IPA) and acetone and were fully oven dried prior to use. This process was repeated to ensure that all surface dirt was removed from the glass. The glass substrates were then placed into a cold walled chemical vapour deposition (CVD) reactor at 500^0C. A piece of metal was loaded into the reaction chamber suspended 8 mm above the glass to ensure laminar flow created by a baffle. The reagents were used as supplied. Titanium (IV) ethoxide was used as a titanium source. The precursor was dissolved in 20 mL of toluene inside a 100 mL round bottom flask. The gas inlet allowed the carrier gas (nitrogen) to pass into the solution and transported the aerosol into the heated reactor at a rate of 1 L/min. The flow rate was controlled by a flow gauge. An ultrasonic humidifier was used to generate the aerosol. The produced film was characterized via X-ray diffraction (XRD) and X-ray

photoelectron spectroscopy (XPS). The XRD pattern was acquired using a Bruker D8 Discover X-ray diffractometer using monochromatic Cu K$\alpha 1$ and Cu K$\alpha 2$ radiation of wavelengths 1.54056 and 1.54439 Å respectively, emitted in an intensity ratio of $2{:}1$ with a voltage of 40 kV and a current of 40 mA. The incident beam angle was $1°$ and data was collected between $10°$ and $66°$ with a step size of $0.05°$ at 1.0 s/step. XPS was conducted on a Thermo Scientific K-alpha spectrometer with monochromated Al Kα radiation, a dual beam charge compensation system and constant pass energy of 50 eV (spot size 400 μm). Survey scans were collected in the binding energy range $0–1200$ eV. High resolution peaks were used for the principal peaks of titanium and oxygen. Data was calibrated against C $1s$ (285.0 eV). Data was fitted using the CASA XPS software. Scanning electron microscopy (SEM) images of SERS and PIERS substrates were obtained using a JEOL JSM 6701 operated with an acceleration voltage of 10 kV.

It is generally accepted that there are different definitions of the SERS EF depending on experimental conditions [36]. Here, the extent of the SERS and PIERS enhancement was quantified by computing the enhancement factor, EF, from an *analytical chemistry point of view* [36] as:

$$EF = \frac{I_{SERS}/N_{SERS}}{I_{Raman}/N_{Bulk}}$$

where I_{SERS} is the intensity of a selected vibrational mode for the analyte peak and I_{Raman} is the intensity of the same vibrational mode of the sample in bulk phase. N_{SERS} is the concentration of analyte adsorbed on the gold particles and N_{Bulk} is the concentration of analyte in the liquid bulk. These values were calculated as follows:

$$N_{SERS} = \frac{C\ V\ N_A\ A_{Raman}}{A_{sub}}$$

$$N_{Bulk} = \frac{\rho\ h\ N_A\ A_{Raman}}{M}$$

where C is the analyte solution concentration, V is the volume of the droplet, N_A is Avogadro's constant, A_{Raman} is the laser spot area ($351.76\ \mathrm{nm}^2$), A_{sub} is the substrate area ($9\ \mathrm{mm}^2$), M is the

molecular weight of the analyte, ρ is the density of the target analyte and h is the confocal depth ($21\ \mu\mathrm{m}$). All enhancement factors are defined with respect to the non-SERS of the same molecule in the same conditions as the SERS experiments.

Results and discussion

Particle growth kinetics

The reactor design procedure starts with the batch study of the synthesis kinetics via *in situ* time-resolved UV-Vis spectroscopy. Recently we demonstrated that kinetics derived from UV-Vis spectroscopy measurements can be employed to guide the design of flow reactors producing gold nanoparticles [41]. Three different seed concentrations were tested, corresponding to $0.007\ \mathrm{mM}$, $0.0008\ \mathrm{mM}$ and $0.00025\ \mathrm{mM}$ $\mathrm{Au}(0)$ in colloidal form, whereas the other parameters were maintained constant. Relevant features of the spectra were extracted to monitor the synthesis evolution (see Fig. 3). In particular, the evolution of the absorbance at $400\ \mathrm{nm}$ (Abs_{400}) is useful to assess when the precursor conversion is completed, as it relates to the amount of $\mathrm{Au}(0)$ present in solution [44,45]. One can hence define the precursor conversion $X(t)$ as: $X(t) = [Abs_{400}(t) - Abs_{400}(t=0)]/[Abs_{400}(t \to +\infty) - Abs_{400}(t=0)]$.

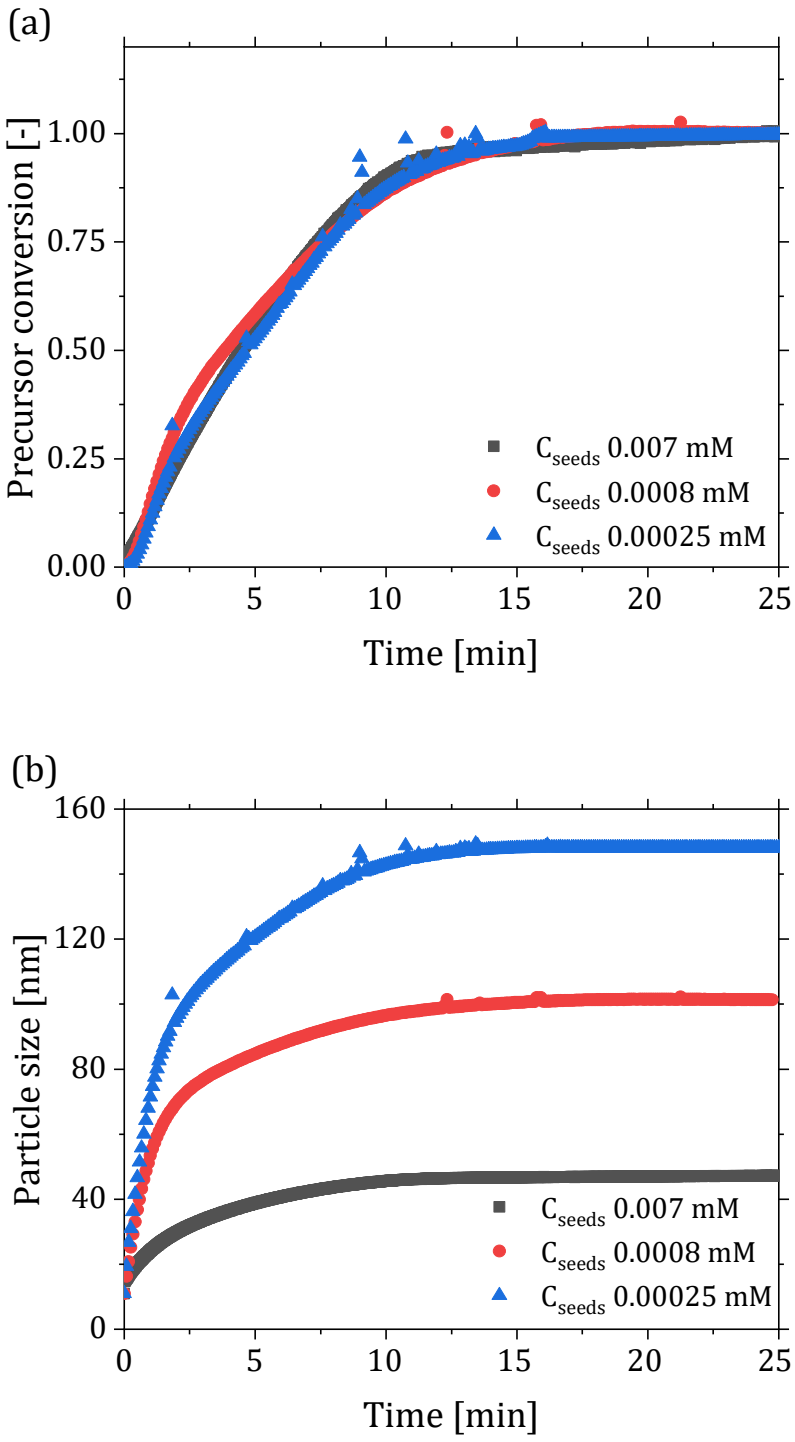

Figure 3. (a) Conversion of precursor X as a function of time for different seed concentrations and (b) particle size evolution over time for the corresponding experiments. The $\mathrm{Au(III)}$, Tris base and H_2O_2 concentrations are maintained constant in all experiments (0.625 mM, 2.5 mM and 0.2 M respectively), whereas the Au seeds concentration is altered ($0.007, 0.0008$ and 0.00025 mM of $\mathrm{Au}(0)$ in colloidal form).

Fig. 3 (a) shows the evolution of the precursor conversion as a function of time for three different seed concentrations. It is worth noting that all the syntheses terminated after approximately $25\ \mathrm{min}$. This value is also consistent with that reported by Li *et al.* [7] determined by *ex situ* UV-Vis measurements. In their work, Li *et al.* demonstrated that this seeded-growth synthesis most likely proceeds through a surface growth process with negligible homogeneous nucleation. This is also supported by the particle size obtained from the batch experiments here reported, as the final size after the growth process corresponds very closely to that obtained assuming constant particle number concentration during the synthesis (Fig. S2). Assuming constant particle number throughout the synthesis, we can translate the precursor conversion curve in Fig. 3 (a) in particle size evolution in time (see SI 3), shown in Fig. 3 (b). Interestingly, the reaction terminates after the same amount of time in all conditions, despite starting from different seed concentrations and leading to different particle sizes. Conventional reaction limited/diffusion limited growth models [46] would not capture this observation, as different initial seed concentration would lead to different growth rates (particularly, faster growth for a higher particle concentration). This observation leads us to suggest the following simple set of reactions to describe the synthesis:

$$2\mathrm{AuCl_4^-} + 3\mathrm{H_2O_2} \xrightarrow{k_1} 2\mathrm{Au(0)} + 8\mathrm{Cl^-} + 3\mathrm{O_2} + 6\mathrm{H^+} \quad \text{(i)}$$

$$\mathrm{nAu(0)} \xrightarrow{k_2} \mathrm{Au_n} \quad \text{(ii)}$$

$$\mathrm{Au_n} + \mathrm{Au\ seeds} \xrightarrow{k_3} \mathrm{larger\ Au\ NP} \quad \text{(iii)}$$

Reaction $\mathrm{(i)}$ provides the monomers required for the growth of the particles through reaction $\mathrm{(ii)}$-$\mathrm{(iii)}$, where the monomers formed in $\mathrm{(i)}$ are incorporated in the seeds leading to particles enlargement. A similar mechanism has been proposed for the synthesis of quantum dots [47,48], where the precursor is first converted to a monomeric unit, through a reaction equivalent to $\mathrm{(i)}$. These monomers can either induce nucleation or attach to growing particles. In reaction $\mathrm{(ii)}$, the $\mathrm{Au(0)}$ atoms formed in $\mathrm{(i)}$ coalesce forming colloidally unstable clusters of gold atoms. These clusters tend to undergo aggregation towards larger (and colloidally stable) particles, as observed in several Au

nanoparticles syntheses [49,50]. We hypothesize that reaction (i) is a slow process leading to the production of $Au(0)$ at low concentrations throughout the whole growth process, which translates in a low concentration of Au_n clusters formed through reaction (ii). The low concentration of gold clusters, combined with the higher aggregation rate between "small" and "large" particles compared to that between two "small" particles [51], eventually lead to the growth of the seeds through reaction (iii) with negligible formation of new particles. Notably, continuous nucleation combined with size-dependant aggregation has already been observed in the formation of silica nanoparticles through the well-established Stöber process, where particle growth and size focusing take place through selective aggregation of continuously formed nuclei with growing particles [51]. Different works report the seedless reduction of $Au(III)$ to Au nanoparticles by H_2O_2 in the absence of seeds through reaction (i) [52–54]. We observed that the pH of the solution drops after reaction completion from 7.2 to 4.4, a decrease consistent with the stoichiometry of reaction (i), supporting the proposed mechanism for $Au(III)$ reduction. The presence of intermediate small Au_n clusters during the growth of Au nanoparticles has recently been observed by Cheng *et al.* [55] via liquid-phase TEM. These intermediates were then incorporated in the Au seeds leading to particle growth.

In the synthesis studied here, Tris base plays a role in the attachment of the formed clusters on the surface of the particles, as shown by Li et al. [7], where an excess of Tris leads to the formation of polygonal particles, probably due to preferential attachment of the atoms along certain crystal facets. Tris also plays a role in regulating the solution pH, relevant for gold precursor speciation, which in turn regulates the precursor reactivity [56], while pH influences the rate of reduction of $Au(III)$ by H_2O_2 [52]. For the overall growth process to take place with the same rate regardless of the seeds concentration, reaction (i) needs to be the rate limiting step, that is, $k_1 \ll k_2$ and $k_1 \ll k_3$. This hypothesis appears reasonable given the tendency of small gold clusters to aggregate forming colloidally stable nanoparticles [49,50] (in the absence of very specific ligands [57]), combined with the low reducing strength of H_2O_2.

The conversion curves in Fig. 3 (a) were fitted using a first order rate equation for reaction (i), *i.e.* $r_{(\mathrm{i})} = -k_1[\mathrm{Au(III)}]$ (the concentration of $\mathrm{H_2O_2}$ is assumed constant as it is in large excess, with $[\mathrm{H_2O_2}]/[\mathrm{Au(III)}] = 320$):

$$X(t) = 1 - e^{-k_1 t} \tag{1}$$

The fitting of the curves in Fig. 3 (a) with eq. (1) renders a value of $k_1 = 3.03 \cdot 10^{-3} s^{-1}$ (Fig. S3).

Then, the size $d(t)$ is given by (see SI 3 for the derivation):

$$d(t) = \left(\frac{C_{\mathrm{Au(III),0}}}{C_{seeds}} X(t) + 1\right)^{\frac{1}{3}} d_{seeds} \tag{2}$$

Where $C_{\mathrm{Au(III),0}}$ is the initial gold precursor molar concentration, C_{seeds} is the molar concentration of $\mathrm{Au}(0)$ atoms as seeds and d_{seeds} is the seed average size.

Growth of Au nanoparticles to target sizes in continuous flowThe use of heptane as segmenting fluid allows us to approximate the reactor as a plug flow reactor (PFR), where all fluid elements travel with the same velocity. With this approximation being valid, we can then write [58] :

$$X(\tau) = X(t) \tag{3}$$
$$d(\tau) = d(t) \tag{4}$$

Where τ is the reactor average residence time. It is convenient to design the reactor to work at full conversion, to improve the economics of the process, as well as to avoid uncontrolled growth of particles in the collection vial. For this reason, we fixed the value of τ to be $25\ \mathrm{min}$ for all the conditions tested. This is because the reaction time depends only on reaction (i), hence for all conditions tested the reaction terminated after the same amount of time. We then changed the value of C_{seeds} (leaving τ unchanged) to obtain different average particle sizes of the product. We tested this approach for the flow synthesis of particles with size of 50, 100 and $150\ \mathrm{nm}$ (replicating the batch

experiments), as well as 75 nm (not tested in batch). Table 1 summarises the conditions employed for each flow growth synthesis, with the results reported in Fig. 4.

Table 1. Conditions used in the different flow growth syntheses.

	Predicted final particle size $[nm]$			
	50	75	100	150
$C_{seeds}[mM]$	0.007	0.002	0.0008	0.00025
$d_{seeds}[nm]$	11	11	11	11
$C_{Au(III),0}$ $[mM]$	0.625	0.625	0.625	0.625
C_{Tris} $[mM]$	2.5	2.5	2.5	2.5
$C_{H_2O_2}$ $[M]$	0.2	0.2	0.2	0.2
τ $[min]$	25	25	25	25

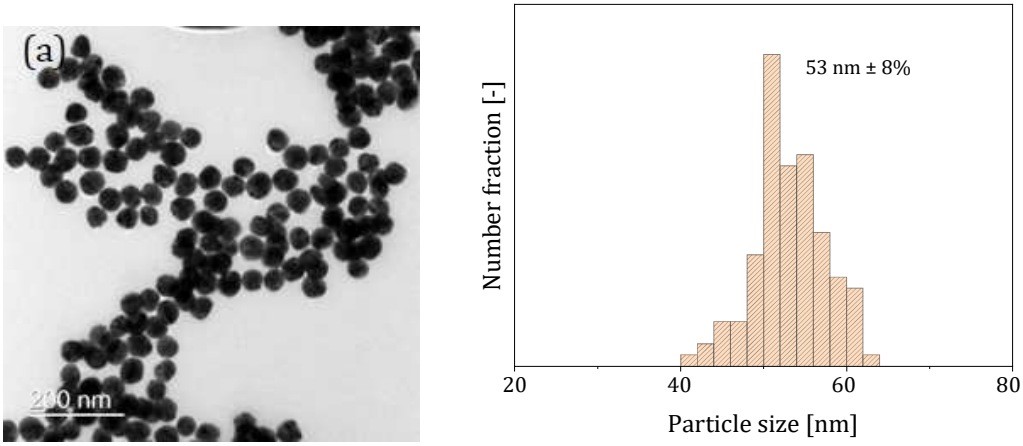

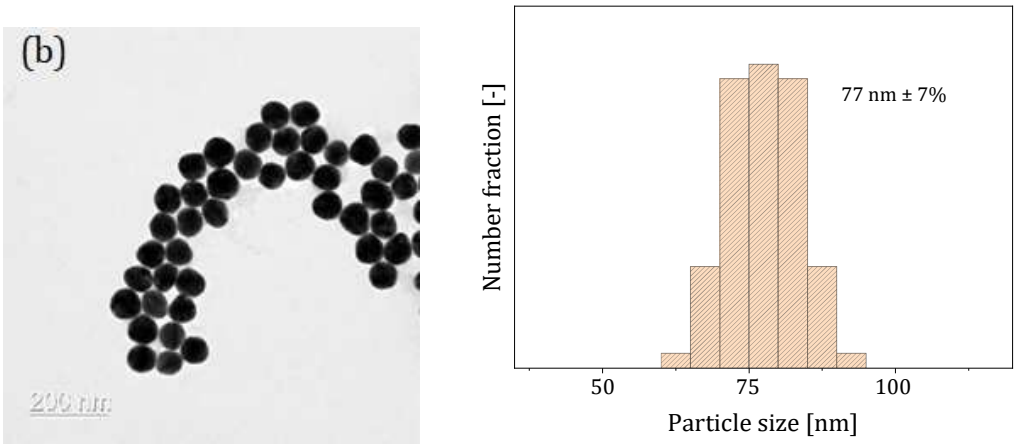

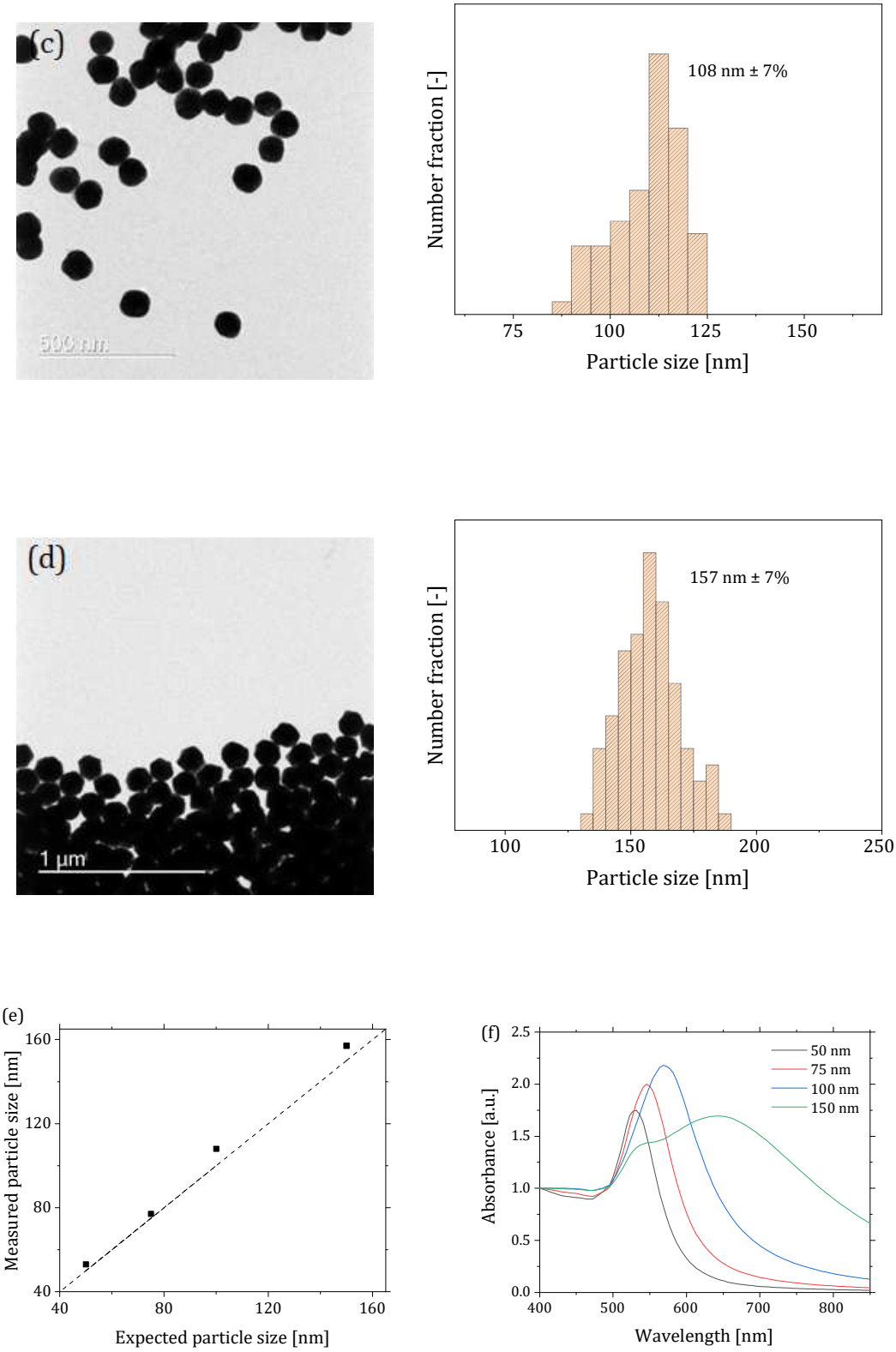

Figure 4. TEM micrographs and particle size distribution for the different size particles synthesised in flow. Conditions used to synthesise the particles are reported in Table 1. (a) Average particle size

53 nm, predicted value 50 nm, (b) average particle size 77 nm, predicted value 75 nm, (c) average particle size 108 nm, predicted value 100 nm, (d) average particle size 157 nm, predicted value 150 nm. (e) Measured against predicted particle size for the different flow syntheses reported. (f) UV-Vis spectra of the four samples produced using the flow reactor (spectra have been normalized over the absorbance at 400 nm).

As Fig. 4 (e) shows, the particle size achieved is close to that theoretically predicted (5 to 8 % deviation). TEM images show that the 50 and the 75 nm particles display good sphericity (Fig. 4 (a)-(b)). As the size increases to 100 nm, a fraction of the particles starts displaying a slightly more polygonal shape (Fig. 4 (c)), feature that gets exacerbated as the size increases to 150 nm (Fig. 4 (d)). This could be related to the increase in the ratio between Tris base and particle concentration as the size increases, since excess Tris base has been reported to decrease the sphericity of the Au nanoparticles [7].

The precursor conversion was measured for all flow syntheses by MP-AES, found to be always above 97% (Fig. S4), as expected from our calculations (full precursor conversion was set as constraint in the reactor design). Fig. 4 (f) shows that the UV-Vis spectra of the particles produced using the flow reactor closely match those theoretically calculated in the literature [8,59] supporting particle monodispersity and absence of aggregates, also observed in the TEM pictures.

It should be noted that the model used to design the reactor is only applicable for spherical particles, while particle anisotropy would require modification of eq. (2). Furthermore, we described the particle populations solely through concentration and average size, which is an approximation appropriate only for narrow size distributions (as in the specific case studied). More refined modelling techniques describing the evolution of the particle size distribution should be implemented when this assumption is not satisfied, such as population balance modelling [47,58,60].

The proposed flow process enables in a single growth step the production of gold nanoparticles up to 150 nm with high monodispersity and uniform shape. Notably, the growth process takes 25 min

regardless of the final desired size: protocols available in the literature leading to uniform spherical particles of size above $50\ \mathrm{nm}$ take as long as few hours with multiple reactant injections required [8,12,13], while faster protocols often lead to a significant fraction of non-spherical particles [9]. One other advantage of the protocol reported is the possibility of working at relatively high Au precursor concentration during the growth step (*i.e.* $0.625\ \mathrm{mM}$), while protocols in the literature usually work at lower precursor concentrations to prevent homogeneous nucleation (in the order of $0.25\ \mathrm{mM}$ or lower) [8,12].

As regards reproducibility, the $50\ \mathrm{nm}$ synthesis was independently repeated three times, *i.e.* repeating both seeds production and subsequent growth. The repeats revealed only 1% change of the average particle size (Fig. S5). The high synthesis reproducibility is a benefit deriving from the use of flow reactors [14], ensured by the tight control of the process parameters in millifluidic systems. In the specific case, it is relevant to highlight the high reproducibility of the seeds synthesis, where the average size of the produced seeds varies $\sim 2\%$ between different runs [41]. Low reproducibility of the seeds synthesis would have significantly affected the reproducibility of the following growth step. The reproducibility values observed in this work match state-of-the-art values for gold nanoparticles [41,61,62], which report these levels of reproducibility for seedless synthesis of Au nanoparticles (with size in the order of $10\ \mathrm{nm}$).

SERS experiments

In order to evaluate the potential use of the produced nanoparticles in SERS and PIERS sensing, experiments were conducted using the $50\ \mathrm{nm}$ particles produced in flow and MBA as a model analyte. MBA represents a common molecule used to test the properties of plasmonic nanoparticles as components of SERS substrates [40]. Furthermore, MBA has been used as part of SERS tags for SERS imaging [27]. Fig. 5 reports the SERS spectra of MBA at various concentration down to $100\ \mathrm{nM}$. The two distinct peaks of MBA at around 1087 and $1595\ \mathrm{cm}^{-1}$, assigned to characteristic aromatic ring vibrations, can be clearly identified in the spectra (highlighted by the red asterisks).

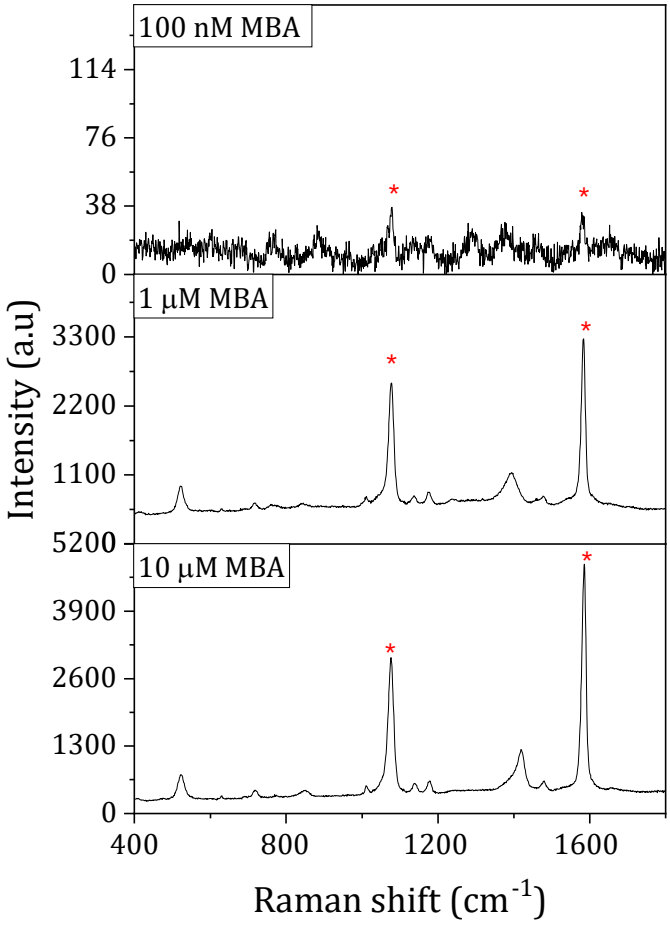

Figure 5. SERS spectra of MBA at different concentrations ranging from 100 nM to 10 μM. The red asterisks highlight the analyte reference peaks.

From a quantitative standpoint, SERS properties of nanomaterials are often evaluated based on their enhancement factor EF. The calculation of the EF is not a straightforward task [36,40]. This parameter should in principle be independent (or weakly dependent) from the probe molecule and representative of the plasmonic enhancement of the SERS signal. In reality the adsorption of the analyte on the nanomaterial surface depends on the affinity of the probe molecule towards the nanomaterial. Hence, following recent trends in the SERS community [40]. MBA was employed as probe to evaluate the EF, due to the high affinity of sulphur (contained in MBA) towards the surface

of Au nanoparticles. SERS EF of $2.37 \cdot 10^7$ and $2.95 \cdot 10^7$ for the peaks at 1087 and 1595 cm^{-1} respectively were calculated (see SI 7). In the literature, values of EF for MBA ranging from 10^3 to 10^7 are reported [63–65]. The EF obtained in this work hence is among the highest found for MBA. The high values of EF observed are attributed to the high monodispersity of the Au nanoparticles, factor promoting close packing of the particles during solution drying, which leads to a high number of hotspots generated in the substrate. SEM images of the particles dried on the microscope glass slide support the last statement (see Fig. S6), with close packing between the particles observed (degree of coverage ~ 372 particles/μm^2). Notably, the substrates used in this work were produced by simply drying the colloidal solution on a microscope slide. Higher values are expected when combining the produced colloidal particles with surfaces designed to promote particle aggregation, leading to closer packing of the Au nanoparticles [66,67].

Given the positive results obtained using MBA, we tested the same particles as substrates for the detection of more challenging analytes, such as the nitro explosives TNT, RDX, PETN and tetryl. Solutions of explosives mixed with AuNPs were deposited onto a glass microscope slide and allowed to dry before analysis. In general, there is good correlation between the peaks observed in the SERS spectra in this study with Raman spectra reported in literature. The key feature in the structures of TNT, RDX, PETN and tetryl is the NO_2 group, observed in its symmetric and asymmetric vibrational modes (discussed below). The SERS spectra of TNT, RDX, PETN and tetryl are shown in Fig. 6.

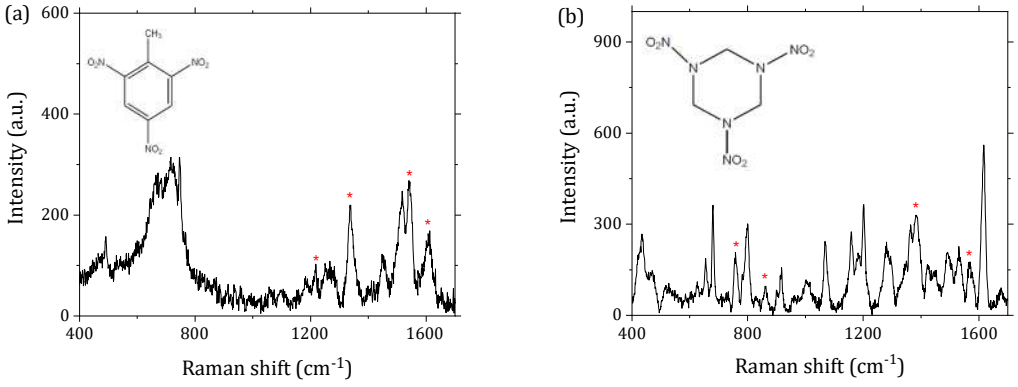

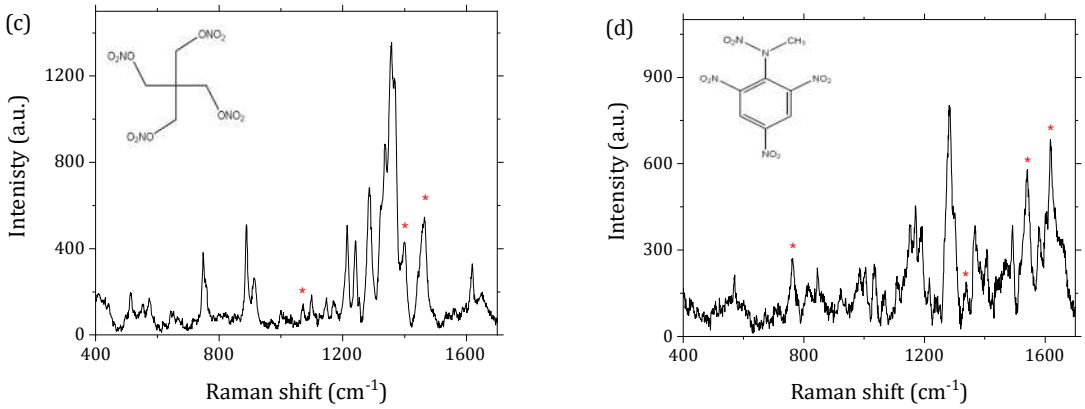

Figure 6. SERS spectra of (a) TNT (2.2 nM), (b) RDX (1.13 µM), (c) PETN (0.79 µM) and (d) tetryl (1.74 mM). The red asterisks highlight the analyte reference peaks, as discussed in the main text.

The graphs show that on addition of Au NPs, a significant number of peaks were observed for all explosives, confirming the enhancement properties from the synthesised Au NPs. A common feature in the structures of all explosives tested is the nitro functional group. The symmetric and asymmetric stretches are the most intense vibrational modes for this group, and typically appear in the ranges of 1260–1400 cm^{-1} and 1500–1650 cm^{-1}, respectively [68]. These stretches can be observed in the SERS spectra. For TNT, the peak observed at 1340 cm^{-1} is attributed to the NO_2 symmetric stretch, 1540 cm^{-1} is attributed to the NO_2 asymmetric stretch, 1220 cm^{-1} to the ring breathing/bending vibrational mode and 1612 cm^{-1} to the C=C ring stretching [69]. For PETN, the peak at 1382 cm^{-1} is attributed to the NO_2 symmetric stretch, that at 1456 cm^{-1} is attributed to the NO_2 asymmetric stretch and the peak at 1074 cm^{-1} is attributed to the C-N stretch [70,71]. For nitramine compounds, the peak between 760-767 cm^{-1} is attributed to the out-of-plane deformation of the nitro group [68]. This was observed in both RDX and tetryl, at 761 cm^{-1} and 763 cm^{-1}, respectively. In addition, Raman band assignments for the other RDX peaks include: the NO_2 symmetric stretch, at 1382 cm^{-1}, the NO_2 asymmetric stretch at 1564 cm^{-1} and the C-N-C ring breathing mode at 864 cm^{-1}. For tetryl, the NO_2 symmetric and asymmetric stretches were observed at 1354 cm^{-1} and 1541 cm^{-1}, respectively. All observed peaks lie very close to SERS studies reported in literature [72–77].

We expanded the use of the 50 nm Au NPs for the detection of biomolecules. We started by studying a relatively simple analyte, glutathione, molecule containing a thiol group that can strongly bind to the surface of Au NPs. Glutathione (GSH) is the most abundant intracellular thiol, with blood concentration in healthy subjects between 0.6 and 3.6 mM [78]. It is an important indicator of cellular health and by evaluating its level in blood it is possible to have an indication of the degree of mitochondrial dysfunction at a tissue level. We tested the Au NPs for the detection of GSH at a concentration of 10 μM (lower concentration than that found in blood/serum). The Raman spectrum is very intricate with many peaks, while the SERS spectra shows distinct bands at 889, 1243, 1280 and 1391 cm^{-1} (Fig. 7 (a)). The most intense ones coming from the amide bond vibrations. Not all bands are intensified equally since the enhancement emerges only when the molecule is in close proximity or directly attached to the active substrate and the enhancement depends on which functional group is attached [79].

To expand the potential target molecules for SERS, glucose was tested as analyte, and successfully detected with the 50 nm gold nanoparticles (Fig. 7 (b)) down to a concentration of 10 μM (for hypoglycaemia and diabetes the concentration of glucose in blood is in the millimolar range, [80] whereas the normal level of glucose in saliva is between 0.1 – 0.3 mM [81]). For this analyte, the $900 - 1200$ cm^{-1} region is often referred to as the fingerprint region; this is dominated by the exo- and endo-cyclic C-O and C-C stretches. It has been noted that this region is difficult to interpret [82]. The Raman spectrum for glucose is rich, but only a few bands can be used as marker bands for the detection and quantification of glucose in blood and plasma samples (*i.e.* the 1125 cm^{-1} band [83]). Furthermore, detection of glucose is more challenging as it does not contain any sulphur atom in its structure, which would ensure a good adsorption on the surface of the particles. On the spectra observed (Fig. 7(b)), some peaks attributed to glucose located at 1073 cm^{-1} and 1125 cm^{-1} were detected down to a concentration of 10 μM, associated with stretching of the C–O bond and bending of the C–OH one . Glucose was successfully detected in the same concentration

reported by Shafer-Peltier *et al.* [84], who employed an Ag film over nanosphere substrate modified with an alkanethiol monolayer to increase the surface affinity of the particles. Focusing on label-free detection, we detected glucose at a lower concentration than Sooraj *et al.* [85], who reported glucose sensing in a range of 0.28 to 288 mM using arrays of silver nanoparticles deposited on a focus ion beam-patterned Si surface.

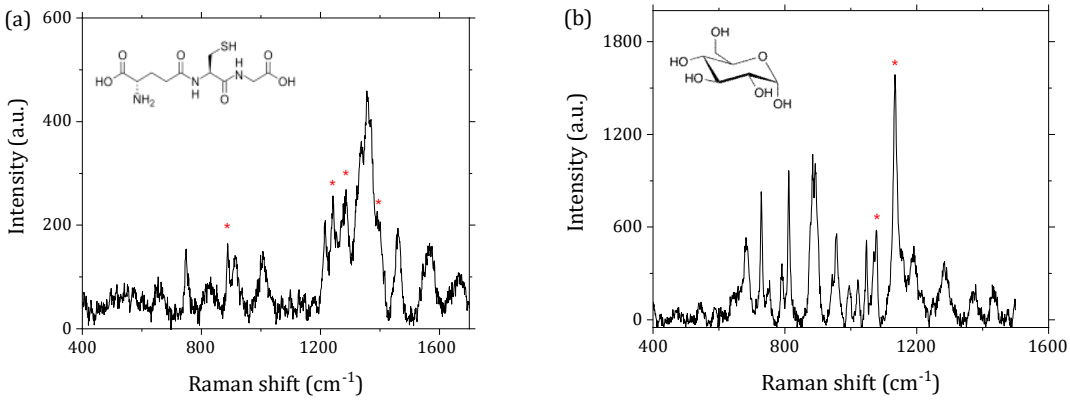

Figure 7. SERS spectra of (a) 10 μM glutathione and (b) 10 μM glucose. The red asterisks highlight the analyte reference peaks, as discussed in the text.

The EF for the various biomolecules and explosives spans between $\sim 10^3$ to 10^7 (see SI 7). This heterogeneity is not surprising, as previously discussed, related to the different affinity of the various analytes towards the particle surface [40].

PIERS experiments

It has been proposed that pre-irradiation of a semiconductor on which plasmonic nanoparticles are deposited gives an enhancement beyond the normal SERS effect: the so-called photo-induced SERS effect (PIERS) [42,43]. The PIERS effect can be used to improve the magnitude of the Raman signals. UV treatment of certain SERS substrates produces oxygen vacancy defects, thus creating sub-band gap trapping sites. Hybrid structures combining noble metals and semiconductors with varying morphologies have also been reported and used for SERS for multi analyte detection. Significant

enhancements can be obtained by using these composite materials which combine the electromagnetic enhancement with the chemical enhancement effects of the semiconductor and adsorbate [86]. TiO_2 composites are usually used as robust, recyclable SERS substrates because of their photo-catalytic degradation of organic pollutants and self-cleaning ability. Recently, Glass *et al*. [43] showed that $50\ nm$ is the optimal size for spherical gold nanoparticles as regards PIERS enhancement. For this reason, we tested the $50\ nm$ particles as substrates for PIERS, drying the mixture of analyte and Au nanoparticles on a TiO_2 thin film (see SI 9 for the film characterization) before irradiation of the composite substrate with UV light. Fig. 8 shows SERS (on TiO_2 surface) and PIERS of MBA as target molecule.

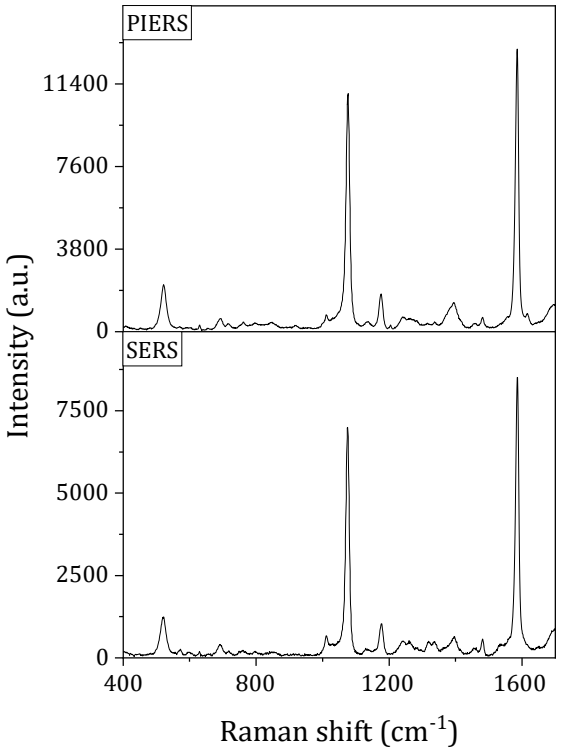

Figure 8. SERS and PIERS spectra of MBA ($1\ \mu M$), using $50\ nm$ Au NPs deposited on a TiO_2 (anatase) thin film. PIERS spectra were recorder after $60\ min$ of exposure to $254\ nm$ UV light.

Micromolar concentration of MBA was successfully detected on TiO_2 anatase thin films at enhanced intensities. The Au NPs contribute to the SERS enhancement through electromagnetic enhancement,

while the TiO_2 contributes through chemical enhancement: this causes an increase in the SERS intensity on TiO_2 compared to that on glass, with the EF increasing from $\sim 3 \cdot 10^7$ to $7 \cdot 10^7$ for both the MBA reference peaks. After UV exposure, the signal enhancement further increased by a factor of ~ 1.6 for both MBA reference peaks, reaching a value of 10^8. SEM images of the Au nanoparticles dried on the TiO_2 thin film showed a degree of packing lower to that observed on the glass slide (film coverage of ~ 136 particles/μm^2). This supports the assertion that the increase in the SERS signal coming from the Au particles dried on the semiconductor film (compared to those coming from the particles dried on the glass slide) is due to chemical enhancement [86]. The further increase in signal after UV radiation is attributed to the PIERS effect, with the light irradiation generating a charge transfer from the semiconductor film to the particles [42]. The ratio between the PIERS and SERS (on TiO_2 film) EFs of approximately 1.6 is consistent with the increases observed by Glass *et al.* [43] using commercially available 50 nm Au nanoparticles deposited on an TiO_2 thin film. Notably, combining the Au nanoparticles with the TiO_2 film (without UV radiation of the substrate) led to a 2.3 times enhancement of the MBA signal compared to that obtained from the particles dried on the glass slide, demonstrating the potential of combining semiconductor thin films with plasmonic nanoparticles towards lowering the detection limits in surface enhanced Raman scattering.

Conclusions

In this work we reported the development of a robust system for on demand production of gold nanoparticles, Au NPs, of controlled average size in the range 50 to 150 nm via a seeded-growth method. The synthesis starts from flow-produced seeds of 11 nm and the seeds are grown to the desired size simply by tuning the seed concentration, while keeping all the other parameters unchanged (*i.e.*, reactant concentrations and temperature). The reactor design and its operation were guided by the study of the growth kinetics via *in situ* time-resolved UV-Vis spectroscopy. These experiments allowed the formulation of a kinetic model that was then applied to set the operating

conditions of the flow reactor, which allowed full precursor conversion in all the conditions tested. The developed flow platform enabled the synthesis of Au nanoparticles over a broad size range, spanning from 50 to 150 nm, corresponding to a window of particle volumes of more than one order of magnitude. Different experiments using different seed samples showed high reproducibility, with only 1% variation of the average particle size obtained after the growth, matching state-of-the-art values for reproducibility of gold nanoparticles synthesis. Compared to other synthetic methods, the process reported enables the synthesis of a variety of monodisperse and spherical gold nanoparticles in a relatively short time with a single growth step. The produced 50 nm Au NPs were tested as components of SERS and PIERS substrates for the detection of different analytes, comprising MBA, a standard analyte useful for SERS imaging, as well as low Raman cross-section materials, including various explosives and biomolecules. These analytes were successfully detected in a label-free fashion down to nM concentrations (depending on the analyte) via SERS, with enhancement factors, EFs, ranging from 10^3 to 10^7 depending on the molecule of interest. The 50 nm particles were also deposited on TiO_2 films and tested for the detection of MBA via PIERS. The use of a semiconductor thin film improved the MBA signal by a factor of ~ 2.3, possibly due to an increase in the chemical enhancement contribution to the overall Raman enhancement. Irradiation with UV light further increased the signal by a factor of 1.6, to an overall almost 4-fold enhancement and an EF of 10^8.

Conflicts of interest

There are no conflicts to declare.

Acknowledgements

LP received funding from the European Union's Horizon 2020 research and innovation programme under the Marie Skłodowska-Curie grant agreement No 721290 http://cosmicetn.eu/. We also thank the EPSRC, U.K. for financial support (EP/M015157/1) through the Manufacturing Advanced Functional Materials (MaFuMa) scheme.

References

[1] V. Myroshnychenko, J. Rodríguez-Fernández, I. Pastoriza-Santos, A.M. Funston, C. Novo, P. Mulvaney, L.M. Liz-Marzán, F.J. García de Abajo, Modelling the optical response of gold nanoparticles, Chem. Soc. Rev. 37 (2008) 1792–1805.

[2] E.C. Dreaden, A.M. Alkilany, X. Huang, C.J. Murphy, M.A. El-Sayed, The golden age: gold nanoparticles for biomedicine, Chem. Soc. Rev. 41 (2012) 2740–2779.

[3] S. Zeng, K.T. Yong, I. Roy, X.Q. Dinh, X. Yu, F. Luan, A Review on Functionalized Gold Nanoparticles for Biosensing Applications, Plasmonics. 6 (2011) 491–506.

[4] A. Corma, H. Garcia, Supported gold nanoparticles as catalysts for organic reactions, Chem. Soc. Rev. 37 (2008) 2096–2126.

[5] M.C.M. Daniel, D. Astruc, Gold Nanoparticles: Assembly, Supramolecular Chemistry, Quantum-Size Related Properties and Applications toward Biology, Catalysis and Nanotechnology, Chem. Rev. 104 (2004) 293–346.

[6] J. Xie, Y. Zheng, J.Y. Ying, Protein-Directed Synthesis of Highly Fluorescent Gold Nanoclusters, J. Am. Chem. Soc. 131 (2009) 888–889.

[7] Y. Li, P. Zhang, J. Duan, S. Ai, H. Li, One-step seeded growth of monodisperse, quasi-spherical, Tris-stabilized gold nanocrystals with sizes from 17 to 325 nm, CrystEngComm. 19 (2017) 318–324.

[8] N.G. Bastus, J. Comenge, V. Puntes, Kinetically Controlled Seeded Growth Synthesis of Citrate-Stabilized Gold Nanoparticles of up to 200 nm : Size Focusing versus Ostwald Ripening, Langmuir. 27 (2011) 11098–11105.

[9] K.R. Brown, M.J. Natan, Hydroxylamine seeding of colloidal Au nanoparticles in solution and on surfaces, Langmuir. 14 (1998) 726–728.

[10] C. Gao, J. Vuong, Q. Zhang, Y. Liu, Y. Yin, One-step seeded growth of Au nanoparticles with widely tunable sizes, Nanoscale. 4 (2012) 2875–2878.

[11] X. Liu, H. Xu, H. Xia, D. Wang, Rapid Seeded Growth of Monodisperse, Quasi-Spherical, Citrate-Stabilized Gold Nanoparticles via H_2O_2 Reduction, Langmuir. 28 (2012) 13720–13726.

[12] J. Polte, M. Herder, R. Erler, S. Rolf, A. Fischer, C. Würth, A.F. Thünemann, R. Kraehnert, F. Emmerling, Mechanistic insights into seeded growth processes of gold nanoparticles, Nanoscale. 2 (2010) 2463–2469.

[13] C. Ziegler, A. Eychm, Seeded Growth Synthesis of Uniform Gold Nanoparticles with Diameters of 15 - 300 nm, J. Phys. Chem. C. 115 (2011) 4502–4506.

[14] S. Marre, K.F. Jensen, Synthesis of micro and nanostructures in microfluidic systems, Chem. Soc. Rev. 39 (2010) 1183–1202.

[15] A.M. Nightingale, J.H. Bannock, S.H. Krishnadasan, F.T.F. O'Mahony, S.A. Haque, J. Sloan, C. Drury, R. Mcintyre, J.C. deMello, Large-scale synthesis of nanocrystals in a multichannel droplet reactor, J. Mater. Chem. A. 1 (2013) 4067–4076.

[16] S.E. Lohse, J.R. Eller, S.T. Sivapalan, M.R. Plews, C.J. Murphy, A Simple Millifluidic Benchtop Reactor System for the High-Throughput Synthesis and Functionalization of Gold Nanoparticles with Different Sizes and Shapes, ACS Nano. 7 (2013) 4135–4150.

[17] H. du Toit, T.J. Macdonald, H. Huang, I.P. Parkin, A. Gavriilidis, Continuous flow synthesis of citrate capped gold nanoparticles using UV induced nucleation, RSC Adv. 7 (2017) 9632–9638.

[18] H. Huang, H. du Toit, S. Ben Jaber, G. Wu, L. Panariello, N.T.K. Thanh, I.P. Parkin, A. Gavriilidis, Rapid Synthesis of Gold Nanoparticles with Carbon Monoxide in a Microfluidic Segmented Flow System, React. Chem. Eng. 4 (2019) 884–890.

[19] H. Huang, H. du Toit, M.O. Besenhard, S. Ben-Jaber, P. Dobson, I. Parkin, A. Gavriilidis, Continuous flow synthesis of ultrasmall gold nanoparticles in a microreactor using trisodium citrate and their SERS performance, Chem. Eng. Sci. 189 (2018) 422–430.

[20] A. Silvestri, L. Lay, R. Psaro, L. Polito, C. Evangelisti, Fluidic Manufacture of Star-Shaped Gold Nanoparticles, Chem. - A Eur. J. 23 (2017) 9732–9735.

[21] M. Marelli, F. Bossola, G. Spinetti, E. Sangalli, V.D. Santo, R. Psaro, L. Polito, Microfluidic Synthesis of Hybrid TiO2-Anisotropic Gold Nanoparticles with Visible and Near-Infrared Activity, ACS Appl. Mater. Interfaces. 12 (2020) 38522–38529.

[22] L. Gomez, V. Sebastian, S. Irusta, A. Ibarra, J. Santamaria, Scaled-up production of plasmonic nanoparticles using microfluidics: from metal precursors to functionalized and sterilized nanoparticles, Lab Chip. 14 (2014) 325–332.

[23] L. Uson, V. Sebastian, M. Arruebo, J. Santamaria, Continuous microfluidic synthesis and functionalization of gold nanorods, Chem. Eng. J. 285 (2016) 286–292.

[24] J.B. Deshpande, A.A. Kulkarni, Reaction Engineering for Continuous Production of Silver Nanoparticles, Chem. Eng. Technol. 41 (2018) 157–167.

[25] B. Pinho, L. Torrente-Murciano, Continuous manufacturing of silver nanoparticles between 5 and 80 nm with rapid online optical size and shape evaluation, React. Chem. Eng. 5 (2020)

[26] H. Ye, X. Xia, Enhancing the sensitivity of colorimetric lateral flow assay (CLFA) through signal amplification techniques, J. Mater. Chem. B. 6 (2018) 7102–7111.

[27] E. Lenzi, D. Jimenez De Aberasturi, L.M. Liz-Marzán, Surface-Enhanced Raman Scattering Tags for Three-Dimensional Bioimaging and Biomarker Detection, ACS Sensors. 4 (2019) 1126–1137.

[28] E.C. Le Ru, P.G. Etchegoin, Single-Molecule Surface-Enhanced Raman Spectroscopy, Annu. Rev. Phys. Chem. 63 (2012) 65–87.

[29] M. Nowak, A. Trojanowska, L. Marciniak, M. Binczyk, T. Runka, B. Tylkowski, R. Jastrzab, Preparation and characterization of long-term stable SERS active materials as potential supports for medical diagnostic, Appl. Surf. Sci. 472 (2019) 93–98.

[30] D.K. Sarfo, E.L. Izake, A.P. O'Mullane, G.A. Ayoko, Fabrication of nanostructured SERS substrates on conductive solid platforms for environmental application, Crit. Rev. Environ. Sci. Technol. 49 (2019) 1294–1329.

[31] A. Hakonen, P.O. Andersson, M. Stenbæk Schmidt, T. Rindzevicius, M. Käll, Explosive and chemical threat detection by surface-enhanced Raman scattering: A review, Anal. Chim. Acta. 893 (2015) 1–13.

[32] K.C. To, S. Ben-Jaber, I.P. Parkin, Recent Developments in the Field of Explosive Trace Detection, ACS Nano. 14 (2020) 10804–10833.

[33] J. Kneipp, H. Kneipp, B. Wittig, K. Kneipp, Novel optical nanosensors for probing and imaging live cells, Nanomedicine Nanotechnology, Biol. Med. 6 (2010) 214–226.

[34] Z. Starowicz, R. Wojnarowska-Nowak, P. Ozga, E.M. Sheregii, The tuning of the plasmon resonance of the metal nanoparticles in terms of the SERS effect, Colloid Polym. Sci. 296 (2018) 1029–1037.

[35] J.A. Creighton, C.G. Blatchford, M.G. Albrecht, Plasma resonance enhancement of Raman scattering by pyridine adsorbed on silver or gold sol particles of size comparable to the excitation wavelength, J. Chem. Soc. Faraday Trans. 2 Mol. Chem. Phys. 75 (1979) 790–798. https://doi.org/10.1039/F29797500790.

[36] E.C. Le Ru, E. Blackie, M. Meyer, P.G. Etchegoint, Surface enhanced Raman scattering enhancement factors: A comprehensive study, J. Phys. Chem. C. 111 (2007) 13794–13803.

[37] M. Moskovits, Surface-enhanced spectroscopy, Rev. Mod. Phys. 57 (1985) 783–826.

[38] E. Le Ru, E. Pablo, Principles of Surface Enhanced Raman Spectroscopy and related plasmonic effects, Elsevier Science, 2009.

[39] D. Cialla, A. März, R. Böhme, F. Theil, K. Weber, M. Schmitt, J. Popp, Surface-enhanced Raman spectroscopy (SERS): Progress and trends, Anal. Bioanal. Chem. 403 (2012) 27–54.

[40] S.E.J. Bell, G. Charron, E. Cortés, J. Kneipp, M.L. de la Chapelle, J. Langer, M. Procházka, V. Tran, S. Schlücker, Towards Reliable and Quantitative Surface-Enhanced Raman Scattering (SERS): From Key Parameters to Good Analytical Practice, Angew. Chemie - Int. Ed. 59 (2020) 5454–5462.

[41] L. Panariello, S. Damilos, H. du Toit, G. Wu, A.N.P. Radhakrishnan, I.P. Parkin, A. Gavriilidis, Highly reproducible, high-yield flow synthesis of gold nanoparticles based on a rational reactor design exploiting the reduction of passivated Au(III), React. Chem. Eng. 5 (2020) 663–676.

[42] S. Ben-Jaber, W.J. Peveler, R. Quesada-Cabrera, E. Cortés, C. Sotelo-Vazquez, N. Abdul-Karim, S.A. Maier, I.P. Parkin, Photo-induced enhanced Raman spectroscopy for universal ultra-trace detection of explosives, pollutants and biomolecules, Nat. Commun. 7 (2016) 1–6.

[43] D. Glass, E. Cortés, S. Ben-Jaber, T. Brick, R. Quesada-Cabrera, W.J. Peveler, Y. Zhu, C.S. Blackman, C.R. Howle, I.P. Parkin, S.A. Maier, Photo-induced enhanced Raman spectroscopy (PIERS): sensing atomic-defects, explosives and biomolecules, Proceeding SPIE. 11010 (2019) 110100D.

[44] T. Hendel, M. Wuithschick, F. Kettemann, A. Birnbaum, K. Rademann, J. Polte, In situ determination of colloidal gold concentrations with UV-Vis spectroscopy: Limitations and perspectives, Anal. Chem. 86 (2014) 11115–11124.

[45] L. Scarabelli, A. Sanchez-Iglesias, J. Perez-Juste, L.M. Liz-Marzán, A " Tips and Tricks " Practical Guide to the Synthesis of Gold Nanorods, J. Phys. Chem. Lett. 6 (2015) 4270–4279.

[46] T. Sugimoto, Monodispersed Particles, Elsevier, Amsterdam, 2001.

[47] S. Lazzari, M. Abolhasani, K.F. Jensen, Modeling of the formation kinetics and size distribution evolution of II-VI Quantum Dots, React. Chem. Eng. 2 (2017) 567–576.

[48] J.Y. Rempel, M.G. Bawendi, K.F. Jensen, Insights into the kinetics of semiconductor nanocrystal nucleation and growth, J. Am. Chem. Soc. 131 (2009) 4479–4489.

[49] J. Polte, T.T. Ahner, F. Delissen, S. Sokolov, F. Emmerling, A.F. Thünemann, R. Kraehnert, Mechanism of Gold Nanoparticle Formation in the Classical Citrate Synthesis Method Derived from Coupled In Situ XANES and SAXS Evaluation, J. Am. Chem. Soc. 132 (2010) 1296–1301.

[50] J. Polte, R. Erler, A.F. Thünemann, S. Sokolov, T.T. Ahner, K. Rademann, F. Emmerling, R.

Kraehnert, Nucleation and Growth of Gold Nanoparticles Studied via in situ Small Angle X-ray Scattering at Millisecond Time Resolution, ACS Nano. 4 (2010) 1076–1082.

[51] G.H. Bogush, C.F. Zukoski IV, Uniform silica particle precipitation: An aggregative growth model, J. Colloid Interface Sci. 142 (1991) 19–34.

[52] B.R. Panda, A. Chattopadhyay, Synthesis of Au nanoparticles at "all" pH by H_2O_2 reduction of $HAuCl_4$, J. Nanosci. Nanotechnol. 7 (2007) 1911–1915.

[53] T.K. Sarma, A. Chattopadhyay, Starch-mediated shape-selective synthesis of Au nanoparticles with tunable longitudinal plasmon resonance, Langmuir. 20 (2004) 3520–3524.

[54] R. De La Rica, M.M. Stevens, Plasmonic ELISA for the ultrasensitive detection of disease biomarkers with the naked eye, Nat. Nanotechnol. 7 (2012) 821–824.

[55] Y. Cheng, J. Tao, G. Zhu, J.A. Soltis, B.A. Legg, E. Nakouzi, J.J. De Yoreo, M.L. Sushko, J. Liu, Near surface nucleation and particle mediated growth of colloidal Au nanocrystals, Nanoscale. 10 (2018) 11907–11912.

[56] M. Wuithschick, A. Birnbaum, S. Witte, M. Sztucki, U. Vainio, N. Pinna, K. Rademann, F. Emmerling, R. Kraehnert, J. Polte, Turkevich in New Robes: Key Questions Answered for the Most Common Gold Nanoparticle Synthesis, ACS Nano. 9 (2015) 7052–7071.

[57] I. Chakraborty, T. Pradeep, Atomically Precise Clusters of Noble Metals: Emerging Link between Atoms and Nanoparticles, Chem. Rev. 117 (2017) 8208–8271.

[58] L. Panariello, L. Mazzei, A. Gavriilidis, Modelling the synthesis of nanoparticles in continuous microreactors: the role of diffusion and residence time distribution on nanoparticle characteristics, Chem. Eng. J. 350 (2018) 1144–1154.

[59] W. Haiss, N.T.K. Thanh, J. Aveyard, D.G. Fernig, Determination of Size and Concentration of Gold Nanoparticles from UV − Vis Spectra Determination of Size and Concentration of Gold Nanoparticles from UV - Vis Spectra, Anal. Chem. 79 (2007) 4215–4221.

[60] S. Lazzari, P.M. Theiler, Y. Shen, C.W. Coley, A. Stemmer, K.F. Jensen, Ligand-Mediated Nanocrystal Growth, Langmuir. 34 (2018) 3307–3315.

[61] F. Kettemann, A. Birnbaum, S. Witte, M. Wuithschick, N. Pinna, R. Kraehnert, K. Rademann, J. Polte, Missing Piece of the Mechanism of the Turkevich Method: The Critical Role of Citrate Protonation, Chem. Mater. 28 (2016) 4072–4081.

[62] F. Schulz, T. Homolka, N.G. Bastús, V. Puntes, H. Weller, T. Vossmeyer, Little adjustments significantly improve the Turkevich synthesis of gold nanoparticles, Langmuir. 30 (2014) 10779–10784.

[63] T.A. Laurence, G.B. Braun, N.O. Reich, M. Moskovits, Robust SERS enhancement factor statistics using rotational correlation spectroscopy, Nano Lett. 12 (2012) 2912–2917.

[64] C.J. Orendorff, A. Gole, T.K. Sau, C.J. Murphy, Surface-enhanced Raman spectroscopy of self-assembled monolayers: Sandwich architecture and nanoparticle shape dependence, Anal. Chem. 77 (2005) 3261–3266.

[65] B. Hu, S.B. Wang, K. Wang, M. Zhang, S.H. Yu, Microwave-assisted rapid facile "green" synthesis of uniform silver nanoparticles: Self-assembly into multilayered films and their optical properties, J. Phys. Chem. C. 112 (2008) 11169–11174.

[66] S. Yang, X. Dai, B.B. Stogin, T.S. Wong, Ultrasensitive surface-enhanced Raman scattering detection in common fluids, Proc. Natl. Acad. Sci. U. S. A. 113 (2016) 268–273.

[67] H. Ko, S. Singamaneni, V. V. Tsukruk, Nanostructured surfaces and assemblies as SERS media, Small. 4 (2008) 1576–1599.

[68] R.W. Beal, T.B. Brill, Vibrational behavior of the -NO 2 group in energetic compounds, Appl. Spectrosc. 59 (2005) 1194–1202.

[69] J. Clarkson, W.E. Smith, D.N. Batchelder, D.A. Smith, A.M. Coats, A theoretical study of the structure and vibrations of 2,4,6-trinitrotolune, J. Mol. Struct. 648 (2003) 203–214.

[70] S. Botti, S. Almaviva, L. Cantarini, A. Palucci, A. Puiu, A. Rufoloni, Trace level detection and identification of nitro-based explosives by surface-enhanced Raman spectroscopy, J. Raman Spectrosc. 44 (2013) 463–468.

[71] E. Finot, T. Brulé, P. Rai, A. Griffart, A. Bouhélier, T. Thundat, Raman and photothermal spectroscopies for explosive detection, Micro- Nanotechnol. Sensors, Syst. Appl. V. 8725 (2013) 872528.

[72] S. Almaviva, S. Botti, L. Cantarini, A. Palucci, A. Puiu, A. Rufoloni, L. Landstrom, F.S. Romolo, Trace detection of explosives and their precursors by surface enhanced Raman spectroscopy, Opt. Photonics Counterterrorism, Crime Fight. Def. VIII. 8546 (2012) 854602.

[73] N.A. Hatab, G. Eres, P.B. Hatzinger, B. Gu, Detection and analysis of cyclotrimethylenetrinitramine (RDX) in environmental samples by surface-enhanced Raman spectroscopy, J. Raman Spectrosc. 41 (2010) 1131–1136.

[74] T. Liyanage, A. Rael, S. Shaffer, S. Zaidi, J. V. Goodpaster, R. Sardar, Fabrication of a self-assembled and flexible SERS nanosensor for explosive detection at parts-per-quadrillion levels from fingerprints, Analyst. 143 (2018) 2012–2022.

[75] X. Wang, S. Chang, J. Yang, J. Tan, H. Jia, H. Yin, X. Li, G. Peng, Detection of TNT in acetone using Raman spectroscopic signature, Int. Symp. Photoelectron. Detect. Imaging 2007 Laser, Ultraviolet, Terahertz Technol. 6622 (2007) 662219.

[76] F. Zapata, M. López-López, C. García-Ruiz, Detection and identification of explosives by surface enhanced Raman scattering, Taylor & Francis, 2016.

[77] S. Botti, L. Cantarini, A. Palucci, Surface-enhanced Raman spectroscopy for trace-level detection of explosives, J. Raman Spectrosc. 41 (2010) 866–869.

[78] T.J. Van 'T Erve, B.A. Wagner, K.K. Ryckman, T.J. Raife, G.R. Buettner, The concentration of glutathione in human erythrocytes is a heritable trait, Free Radic. Biol. Med. 65 (2013) 742–749.

[79] G.G. Huang, X.X. Han, M.K. Hossain, Y. Kitahama, Y. Ozaki, A study of glutathione molecules adsorbed on silver surfaces under different chemical environments by surface-enhanced Raman scattering in combination with the heat-induced sensing method, Appl. Spectrosc. 64 (2010) 1100–1108.

[80] C. Kapitza, T. Forst, H. V. Coester, F. Poitiers, P. Ruus, A. Hincelin-Méry, Pharmacodynamic characteristics of lixisenatide once daily versus liraglutide once daily in patients with type 2 diabetes insufficiently controlled on metformin, Diabetes, Obes. Metab. 15 (2013) 642–649.

[81] I. Al-Ogaidi, H. Gou, A.K.A. Al-kazaz, Z.P. Aguilar, A.K. Melconian, P. Zheng, N. Wu, A gold@silica core-shell nanoparticle-based surface-enhanced Raman scattering biosensor for label-free glucose detection, Anal. Chim. Acta. 811 (2014) 76–80.

[82] A.F. Bell, L.D. Barron, L. Hecht, Vibrational Raman optical activity study of D-glucose, Carbohydr. Res. 257 (1994) 11–24.

[83] K. Virkler, I.K. Lednev, Raman spectroscopy offers great potential for the nondestructive confirmatory identification of body fluids, Forensic Sci. Int. 181 (2008) e1–e5.

[84] K.E. Shafer-Peltier, C.L. Haynes, M.R. Glucksberg, R.P. Van Duyne, Toward a glucose biosensor based on surface-enhanced Raman scattering, J. Am. Chem. Soc. 125 (2003) 588–593.

[85] K.P. Sooraj, M. Ranjan, R. Rao, S. Mukherjee, SERS based detection of glucose with lower concentration than blood glucose level using plasmonic nanoparticle arrays, Appl. Surf. Sci. 447 (2018) 576–581.

[86] H. Fang, C.X. Zhang, L. Liu, Y.M. Zhao, H.J. Xu, Recyclable three-dimensional Ag nanoparticle-decorated TiO2 nanorod arrays for surface-enhanced Raman scattering, Biosens. Bioelectron. 64 (2015) 434–441.